



This is a repository copy of *Barriers to electro dialysis implementation: maldistribution and its impact on resistance and limiting current density*.

White Rose Research Online URL for this paper:

<https://eprints.whiterose.ac.uk/220670/>

Version: Accepted Version

Article:

Ledingham, J., Sedransk Campbell, K.L., In 't Veen, B. et al. (2 more authors) (2022) Barriers to electro dialysis implementation: maldistribution and its impact on resistance and limiting current density. *Desalination*, 531. 115691. ISSN 0011-9164

<https://doi.org/10.1016/j.desal.2022.115691>

Article available under the terms of the CC-BY-NC-ND licence (<https://creativecommons.org/licenses/by-nc-nd/4.0/>).

Reuse

This article is distributed under the terms of the Creative Commons Attribution-NonCommercial-NoDerivs (CC BY-NC-ND) licence. This licence only allows you to download this work and share it with others as long as you credit the authors, but you can't change the article in any way or use it commercially. More information and the full terms of the licence here: <https://creativecommons.org/licenses/>

Takedown

If you consider content in White Rose Research Online to be in breach of UK law, please notify us by emailing eprints@whiterose.ac.uk including the URL of the record and the reason for the withdrawal request.



eprints@whiterose.ac.uk
<https://eprints.whiterose.ac.uk/>

Barriers to electro dialysis implementation: maldistribution and its impact on resistance and limiting current density

Jack Ledingham^{a,1}, Kyra L. Sedransk Campbell^a, Ben In 't Veen^b, Lucas Keyzer^b, Alasdair N. Campbell^a,

^a Department of Chemical and Biological Engineering, The University of Sheffield, Sheffield, S1 4AA, United Kingdom

^b Shell Global Solutions International B.V

¹ Present address

Highlights:

- Fluid dynamics simulations in 3D uncovered significant flow maldistribution in ED
- A rigorous analytical model captured maldistribution through a dimensionless metric
- Stack design and operation significantly impact maldistribution
- There is a detrimental effect on both limiting current density and stack resistance
- The effect on limiting current density is much greater than resistance

Abstract: Electro dialysis is an emerging low-energy membrane-based water-treatment technology with strong potential for industrial use. However, various engineering challenges have prevented widespread utilisation. The flow maldistribution in electro dialysis has been evaluated through computational fluid dynamics simulations in Ansys Fluent. A typical lab-scale stack geometry with ten cell pairs was simulated, and significant flow non-uniformity was found. An analytical model showed good agreement with simulations and was used to quantify the maldistribution through a single dimensionless number. The inlet flow rate and stack geometry were varied to investigate the distribution of flow. Maldistribution was exacerbated when the inlet flow rate, channel width, distributor angle, or number of cell pairs was increased. Further, the effect of maldistribution on the limiting current density (LCD) and stack resistance was evaluated using a one-dimensional model. Maldistribution was found to significantly impact the LCD, with a reduction of 23% found for the typical geometry relative to uniformly distributed flow. The resistance was impacted much less, showing an increase in resistance of only 2%. This highlights that maldistribution is a localised issue rather than a global one and goes some way to explaining why there has been a distinct lack of research into flow maldistribution in electro dialysis.

29 Keywords: Electrodialysis, computational fluid dynamics, flow maldistribution, limiting current density

30

31 Corresponding authors at: Department of Chemical and Biological Engineering, The University of Sheffield,

32 Sheffield, S1 4AA, United Kingdom.

33 Email: jsplodingham@sheffield.ac.uk (Jack Ledingham)

34 1. Introduction

35 Electrodialysis (ED) is an emerging electromembrane technology with broad applications in salt separation processes
36 such as desalination, resource recovery, and wastewater treatment [1]. As the global water crisis worsens, it is
37 becoming more important to conserve natural freshwater resources [2]. Brackish water and brine desalination can
38 provide an alternate source for potable water, and the removal of pollutants from industrial and municipal
39 wastewaters prevents the contamination of already depleting sources of freshwater. Currently, reverse osmosis (RO)
40 is the most common form of water treatment due to its reliability and ease of membrane manufacturing [3]. There
41 are many inherent advantages to ED over RO, stemming from the fact that in ED, it is the minority species (the salt)
42 which is transported, whereas in RO it is the majority species (water) [4]. These advantages therefore include a higher
43 rate of separation, lower susceptibility to fouling, greater membrane lifespan, and a higher recovery ratio. The high
44 customisability of ED using alternative membrane types has led to a great many potential applications such as the
45 use of bipolar membranes to change the pH of a stream by electrochemical means. However, significant engineering
46 challenges underpinning ED limit their efficacy. Elimination of these challenges would ensure greater prevalence
47 throughout industry as well as drive process electrification.

48 In ED, a potential difference is employed to drive the transport of ions through ion exchange membranes (IEMs) [5].
49 These act as semi-permeable barriers, theoretically permitting the selective transport of either cations or anions only,
50 depending on the identity of the fixed charges in the membrane pores. In conventional ED, anion and cation exchange
51 membranes (AEMs and CEMs) are layered in an alternating pattern, creating channels through which salt solutions
52 flow (Figure 1a). The electric field drives ion transport from one channel (diluate), through the appropriate IEM and
53 into the other (concentrate) (Figure 1b). Several sets of membranes and channels (cell pairs) are held between two
54 electrodes, comprising the separation system referred to as an ED stack.

55 Recent advances in IEM technology have improved performance and reduced costs to the point where large scale
56 ED applications are becoming commercially viable [6]. An analysis of 100 recent ED publications (published
57 between 15/02/21 and 15/11/21) revealed that most papers (68%) focus on applications of ED to new systems, or in
58 conjunction with other technologies. Novel membrane manufacturing was the next most prevalent (15%), with
59 foundational research (10%) and model development (7%) being the least. The overwhelming focus on the proof-of-
60 concept for new applications is characteristic of an emerging technology, but the depth of this research is limited
61 since understanding of underlying ED phenomena is incomplete. This can be seen from the wide use of empirical
62 models to analyse ED behaviour and predict the LCD rather than phenomenological ones. Models are resultantly
63 accurate only for the system they were derived for and global ED insights cannot be ascertained. The fundamentals

64 of ED underpin all aspects of operation, and so a lack of insight limits the extent of optimisation that is achievable.
65 There is therefore significant value in building knowledge through mathematical modelling and foundational studies.
66 Reducing inefficiencies and improving overall performance and robustness will lead to greater uptake of ED
67 throughout industry for the applications investigated in the published literature [7–11]. Resultantly, the inherent
68 benefits of ED as a separation technology could be realised for both industrial and municipal applications.

69 One ubiquitous assumption in both ED modelling and experimental data analysis is that of channel uniformity. This
70 allows for simplification of models to consider only one channel or cell pair, the results of which can be scaled to
71 infer conclusions about global stack performance. In the case of computational fluid dynamics (CFD) models which
72 utilise the Nernst-Planck equation, this greatly decreases computational expense. However, the validity of this
73 assumption has seldom been explored. Gurreri *et al* [12] simulated a 50 cell-pair stack in two dimensions (2D) with
74 0.2 mm thick channels and 0.5 mm width manifolds, and found significant flow maldistribution. It was concluded
75 that a more homogeneous distribution can be obtained by increasing channel pressure drop, decreasing manifold
76 hydraulic losses, and reducing total flow rate. While these insights are valuable, the geometry of the manifold and
77 distributors cannot be accurately represented in 2D, and so conclusions about real ED operation are extrapolations.
78 Cruz-Diaz *et al* [13] investigated the effect of the manifold on flow distribution in a single three-dimensional (3D)
79 channel through tracer-based residence time distribution (RTD) experiments and CFD modelling. It was found that
80 assuming homogeneous flow with dispersion did not accurately predict RTD results, but a segregated flow laminar
81 model did. These studies identified that flow distribution both between channels and within a single channel is not
82 uniform, and that the geometry of the stack has a significant effect on maldistribution for simplified cases. This study
83 aims to expand this to a more accurate representation of an ED stack and study the effects of maldistribution in
84 greater depth.

85 Significant insight into the flow distribution in ED stacks is found by considering investigations into plate-and-frame
86 heat exchangers (PFHEX) due to their analogous geometries. The study of flow maldistribution in PFHEX and fuel
87 cells is frequently studied [14], often using CFD to also understand its effects on operation [15–22]. One useful result
88 from these studies is an analytical flow distribution model developed by Bassiouny and Martin [20]. A dimensionless
89 number, m , is used to quantify the extent of maldistribution and to recreate the channel velocity distribution given
90 appropriate geometrical and operating parameters. The details of the model are found in section 2.2.

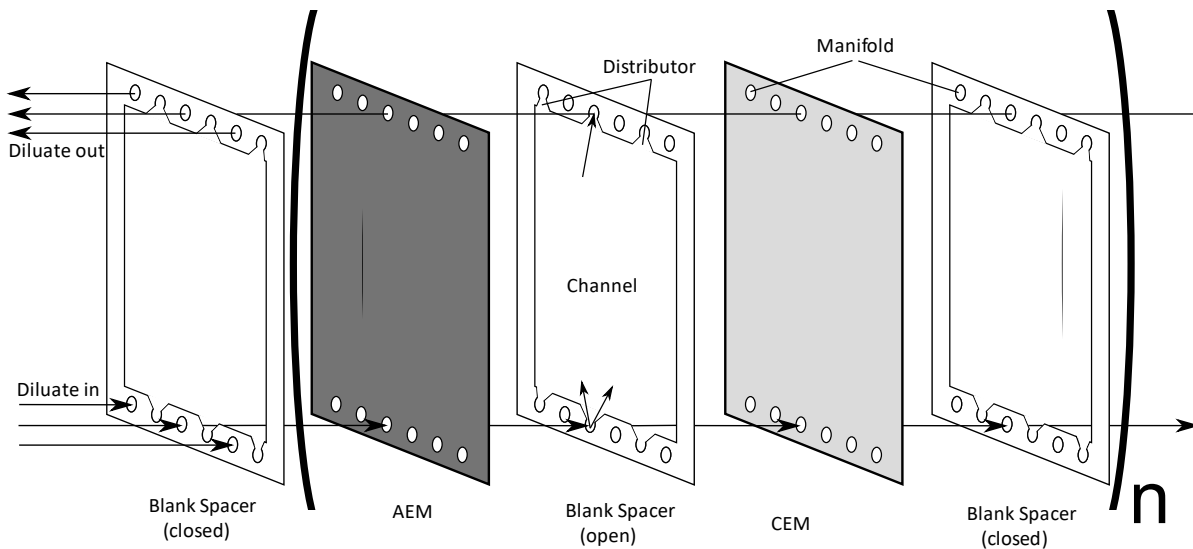
91 Analysing the effect of maldistribution on ED is crucial to ascertain the extent to which operational efficiency is
92 impacted. One key performance metric is the limiting current density (LCD). In ED, transport is fastest in the IEMs

93 due to the high ion concentration, and so ions deplete at the diluting side of the membrane and accumulate at the
94 concentrating side through a process known as concentration polarisation [23] (Figure 1c). The magnitude of
95 concentration polarisation grows as the applied voltage and ion flux are increased. A point is reached where the
96 concentration at the diluting side of the membrane vanishes, and the flux of ions cannot be increased further. This is
97 referred to as the LCD and is associated with a large increase in electrical resistance. Increasing the voltage beyond
98 this point induces water-splitting to provide additional ion flux, leading to wasted energy and undesired changes in
99 the pH of streams. It is therefore imperative to operate below the LCD, with any reduction in it having significant
100 consequences for process intensification. The LCD is reached when the interfacial concentration anywhere vanishes,
101 which occurs first in the slowest channel where the residence time and ion depletion are the greatest. The effect of
102 maldistribution on LCD was studied by Tanaka [24–26], assuming a normal distribution of the stack velocity. The
103 standard deviation was used as a quantification of maldistribution when calculating the LCD, and the minimum
104 velocity was assumed to be three standard deviations below the mean. This approach is, however, at odds with the
105 maldistribution model of Bassiouny and Martin [20], which suggests a hyperbolic-cosine distribution. The strengths
106 of these two approaches to maldistribution will be combined in this study to provide a dimensionless measure for
107 maldistribution in ED, which is then used as a more rigorous metric when determining the impact on the LCD.

108 Variation in residence times between channels has the potential to be very detrimental to ED performance and thus
109 this research is of great value. Beyond the studies mentioned, the presence and consequences of maldistribution have
110 been neglected in published ED models. This study aims to quantify flow maldistribution in an ED stack using a
111 dimensionless number, as well as how it is affected by geometrical and operating parameters. Crucially,
112 quantification of the effect maldistribution has on overall stack resistance and limiting current density is also
113 investigated. Three-dimensional fluid dynamics simulations in ANSYS Fluent were conducted on a representative
114 lab-scale ED stack (Figure 1d). Several aspects of the flow geometry including channel width, manifold area,
115 distributor angle and the number of cell pairs were varied independently to investigate the effect on maldistribution.
116 The inlet stack flow rate was also varied. An analytical model adapted from Bassiouny and Martin [20] is used to
117 quantify and compare the extent of the maldistribution through a dimensionless number, with centreline channel
118 velocities used as the basis of comparison. Furthermore, the effect of maldistribution on ED operation through the
119 LCD and overall stack resistance is determined through a one-dimensional model.

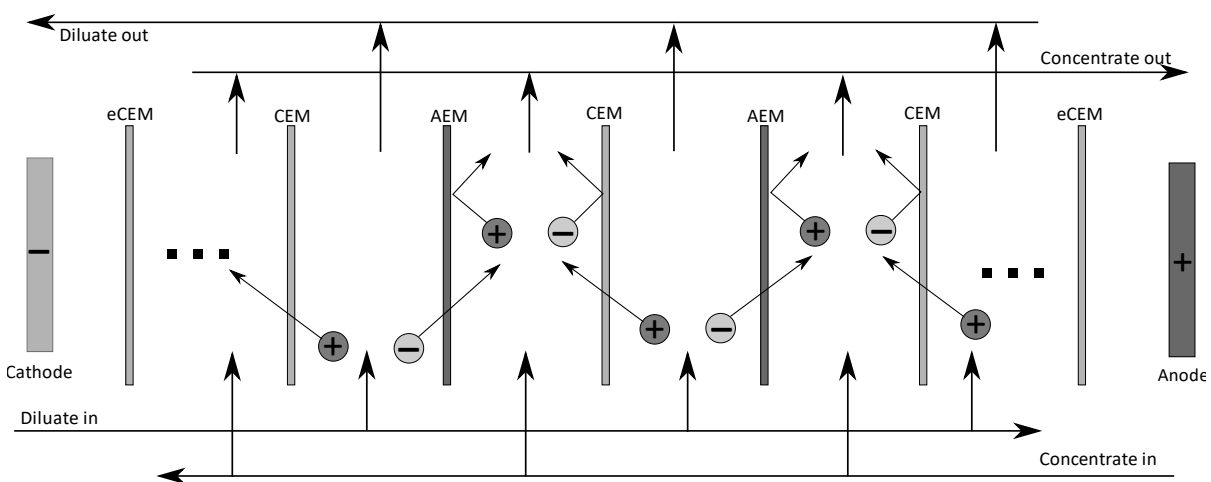
120

(a)



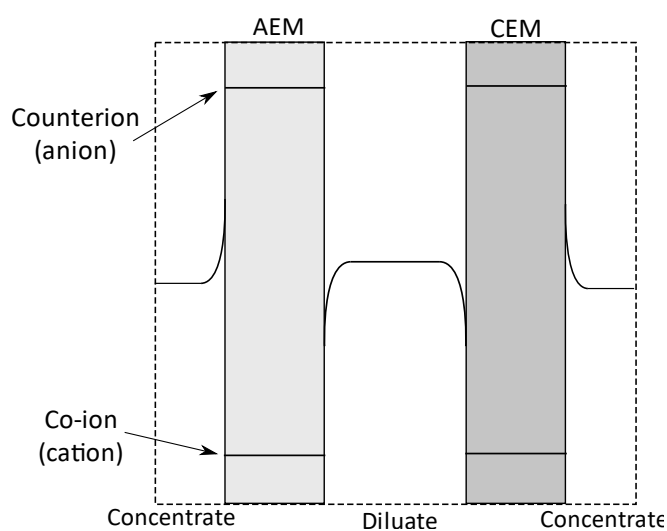
121

(b)



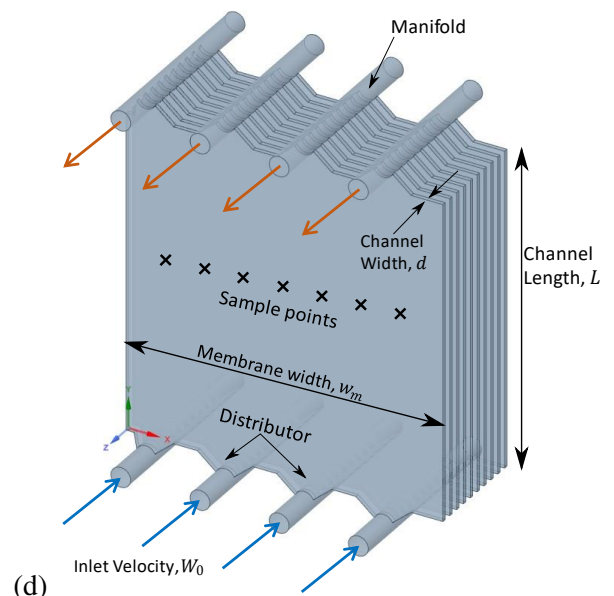
122

(c)



123

(d)



124

125

126

127

128

129

130

Figure 1. a) A schematic representation of a single repeating unit of ED stack, with n being the number of cell pairs. Flow enters and exits from the left-hand side and is distributed to every other channel through open spacer distributors. For simplicity, the concentrate stream is not shown, this would enter through the right-hand side. b) A schematic of ion transport in ED, indicating the repeating pattern of cation and anion exchange membranes as well as the electrodes and end cation exchange membranes (eCEM). Dark shades show positive charges (cations, AEMs, anode) and light shades show negative charges (anions, CEMs, cathode). c) A schematic representation of concentration polarisation. Lines represent the concentration at a given horizontal point, and the vertical height represents the concentration. d) The geometry of a typical lab scale geometry which was used in Fluent CFD simulations. This is the flow region of one stream only, the second being rotationally symmetric to the first. Also shown are the named domains, dimensions and the locations of centreline velocity sample points.

2. Model Development

2.1. Ansys Fluent CFD Model

ANSYS Fluent 2020 R2 was used in this study to generate 3D flow profiles for an ED stack while varying the flow rate and geometry. A bench-scale ED stack with ten cell pairs was selected as this is by far the most common studied in published literature. It is also the simplest geometry that can be simulated while still being representative of a what is practically used at larger scales. Analogies will be drawn to pilot and industrial scale stacks, which tend to have much higher flow rates, a smaller number of large manifolds, a much greater size, a length to width (L/D) ratio of 2.0 (bench scale is typically 1.0) and many more channels, on the order of 50-200. However, different scale stacks do have a similar intermembrane spacing of 0.8 mm to 1.0 mm. A typical lab-scale ED geometry (Figure 1d) consists of cylindrical manifolds used to distribute the fluid feed to the channels (bottom) and collect the treated streams (top). Distributors at the bottom and top of the channel connect it to the manifold and tend to vary significantly in shape. It should be noted that only one of the two streams was simulated, as the two flow regions are rotationally symmetrical. The standard case geometry used in simulations (Figure 1d) has channel dimensions of 1 mm by 80 mm by 80 mm, a distributor angle of 90°, and four manifolds, each of diameter 5 mm. The standard inlet flow rate was 45 L/h, equivalent to an inlet velocity of 0.159 m/s, and liquid water was chosen as the simulated fluid. These values were chosen to represent the geometry of that used in lab-scale ED stacks commercially manufactured for academic research.

To generate the flow profiles, Fluent solves the Navier-Stokes and continuity equations to account for conservation of momentum and mass, respectively.

$$\rho \frac{\partial \mathbf{v}}{\partial t} + \rho (\mathbf{v} \cdot \nabla) \mathbf{v} = \rho \mathbf{g} - \nabla P + \mu \nabla^2 \mathbf{v} \quad (1)$$

$$\frac{\partial \rho}{\partial t} + \nabla(\rho \mathbf{v}) = 0 \quad (2)$$

Here, \mathbf{v} is the vector velocity, ρ and μ are the fluid density and viscosity, respectively, \mathbf{g} is the gravitational acceleration vector, and P is the pressure. The flow was assumed to be steady and laminar to decrease model complexity. Reynolds numbers were calculated post-simulation and were found to be approximately 30 in channels and a maximum of 1000 in the manifolds, which quickly drops as flow is distributed to the channels. Critical Reynolds numbers for spacer-filled channels have been reported at between 140 and 1800 [27,28]. Since the channels simulated in this study are spacer-free, the transitional Reynold's number is likely much higher. Manifold flow is analogous to pipe flow, and so the critical Reynolds number is 2300. Simulations using k-epsilon turbulence

157 modelling gave near-identical flow fields to ones using laminar solvers. The assumption of laminar flow is therefore
 158 valid.

159 Boundary conditions of a given inlet velocity, zero wall velocity and zero outlet gauge pressure were applied:

$$\mathbf{v}|_0 = \hat{\mathbf{n}} W_0 \quad \mathbf{v}|_w = 0 \quad P|_e = 0 \quad (3, 4, 5)$$

160 Here, W_0 is the stack inlet velocity, $\hat{\mathbf{n}}$ is the unit vector normal to the inlet surface, and the subscripts 0, e, and w
 161 refer to the inlet, outlet, and wall boundaries, respectively. Channel velocities were obtained by sampling a
 162 distribution of seven points across the centreline of the channel at 10 mm intervals on rake surfaces. The mean of
 163 these seven points gave a value for the average channel centreline velocity. Table 1 shows the geometrical parameters
 164 varied independently. Where appropriate, the inlet velocity was adjusted to maintain a constant flow rate across all
 165 channels of 4.5 L/h.

166 *Table 1. The operating and geometrical parameters independently varied for the simulations. The range of variation is given along with the nominal value at*
 167 *which a parameter is set while others are adjusted.*

Parameter	Range	Nominal	
Inlet velocity	0.04 – 0.32	0.16	m/s
Channel Width	0.2 – 1.8	1.0	mm
Distributor angle	0 – 180	90	°
Number of manifolds	2 - 6	4	
Number of cell pairs	10 - 45	10	
Length-to-width ratio	1,2	1	

171 Fluent auto-meshing was used to construct the simulation mesh with 2.4 million polyhedral cells used for the standard
 172 case. This was found to be appropriate by conducting simulations on a range of mesh densities and selecting the
 173 smallest number of cells (*i.e.*, the least computationally demanding) which showed a minimal difference to meshes
 174 with higher densities.

175 2.2. Dimensionless Maldistribution Model

176 Determining the flow distribution in ED through CFD simulations is computationally demanding, with the nominal
 177 case simulation taking approximately 1.5 hours to solve. Therefore, an analytical model which uses a single,
 178 predictable dimensionless number to describe the maldistribution would be invaluable. A model for the distribution
 179 of flow in ED was adapted from one developed by Bassiouny and Martin [20] for a PFHEX. The model is based on
 180 mass and momentum balances, taken around junctions between the channels and the feed and exhaust manifolds
 181 (Figure 2a). It is assumed that the (vertical) z -component of the channel velocity is equal to the manifold velocity for
 182 the feed, and zero for the exhaust. For the PFHEX, the impact of this assumption was tested by comparing the results
 183 of models which did and did not consider it. Both approaches gave similar answers, demonstrating that this
 184 assumption is appropriate.

185 Combination of the mass and momentum balances and subsequent conversion into dimensionless form results in the
 186 following second order differential equation.

$$\frac{d^2w}{dz^2} - m^2w = 0 \quad (6)$$

187 Here, w is the dimensionless manifold axial velocity, normalised to the inlet velocity (W_0), z is the dimensionless
 188 axial coordinate, normalised to the manifold length (L), and m is the maldistribution number. The following equation
 189 defines m :

$$m^2 = \left(\frac{nA_c}{A_m}\right)^2 \frac{1}{\zeta} \quad (7)$$

190 Here, n is the total number of channels, A_c and A_m are the cross-sectional areas of the channel and manifold,
 191 respectively, and ζ is the general friction coefficient, which is found through the mean channel pressure drop (ΔP_{mc})
 192 and velocity (U_{mc}) [21].

$$\zeta = \frac{2\Delta P_{mc}}{\rho U_{mc}^2} \quad (8)$$

193 The general friction coefficient is related to the Darcy friction factor (f_D) through the channel length (L) and the
 194 hydraulic diameter (d_h).

$$f_d = \zeta \cdot \frac{d_h}{L} \quad (9)$$

195 The boundary conditions used to solve Eq. (6) are the non-dimensional inlet velocity ($w(0) = 1$) and the fact that
 196 the flow at the far end of the manifold is zero ($w(1) = 0$). The value of m^2 determines the curvature of the profile
 197 connecting the two boundary points, with higher values leading to greater curvature (Figure 2b). This is related to
 198 the distribution of channel velocities through the dimensionless mass balance

$$u_c = -\left(\frac{A_m}{n A_c}\right) \frac{dw}{dz} \quad (10)$$

199 where u_c is the dimensionless channel velocity, normalised to the manifold inlet velocity (W_0). A higher value of m
 200 leads to greater curvature of the axial velocity profile, which leads to a wider distribution of u_c and hence more
 201 maldistribution.

202 Eq. (6) can be solved analytically, assuming m^2 is positive. The equation for $w(z)$ can then be differentiated to one
 203 for $u_c(z)$ using Eq. (10), and dimensional variables can be reintroduced to give an equation for the channel velocity.

$$u_c = U_c/W_0 \quad z = Z/L \quad w = W/W_0 \quad (11,12,13)$$

$$u_c = \left(\frac{A_m}{n A_c} \right) \frac{m \cosh(m(1-z))}{\sinh(m)} \quad (14)$$

$$U_c = W_0 \left(\frac{A_m}{n A_c} \right) \frac{m \cosh(m(1-Z/L))}{\sinh(m)} \quad (15)$$

204 Eq. (15) gives a simple analytic expression for the distribution of flow between channels. The ratio between the
 205 velocity of the fastest channel ($Z = 0 \mid z = 0$) and the slowest channel ($Z = L \mid z = 1$), is determined from Eq. (15)
 206 to be simply $\cosh(m)$, further highlighting the power of m to describe maldistribution.

207 The strength of this model is that it allows for a single non-dimensional number to quantify flow maldistribution
 208 which has a well-defined and rigorous physical basis. Further, m retains enough information to reconstruct velocity
 209 distribution profiles using minimal geometric data and the inlet velocity. Below, the model will be fit to a simulation
 210 of a 3D ED stack for the first time to test the applicability of this potentially powerful model and then to quantify the
 211 extent of maldistribution. Importantly, m can be used in ED process design or targeted models to calculate the LCD
 212 and resistance as the independent variable. This is superior to other maldistribution metrics such as the standard
 213 deviation or percentage-difference between the fastest and slowest channels, which do not have a physical basis and
 214 are therefore of limited practical use.

215 The centreline channel velocities are calculated in Fluent (Section 2.1) and exported to MATLAB R2020b. The
 216 function 'lsqnonlin', a least-squares non-linear optimisation tool was used to obtain a best fit of the model to the flow
 217 profiles, tuning the values of m and W_0 . Fitted velocity distribution profiles could then be compared those simulated
 218 in Fluent, and the value of m used as a non-dimensional metric for the degree of maldistribution.

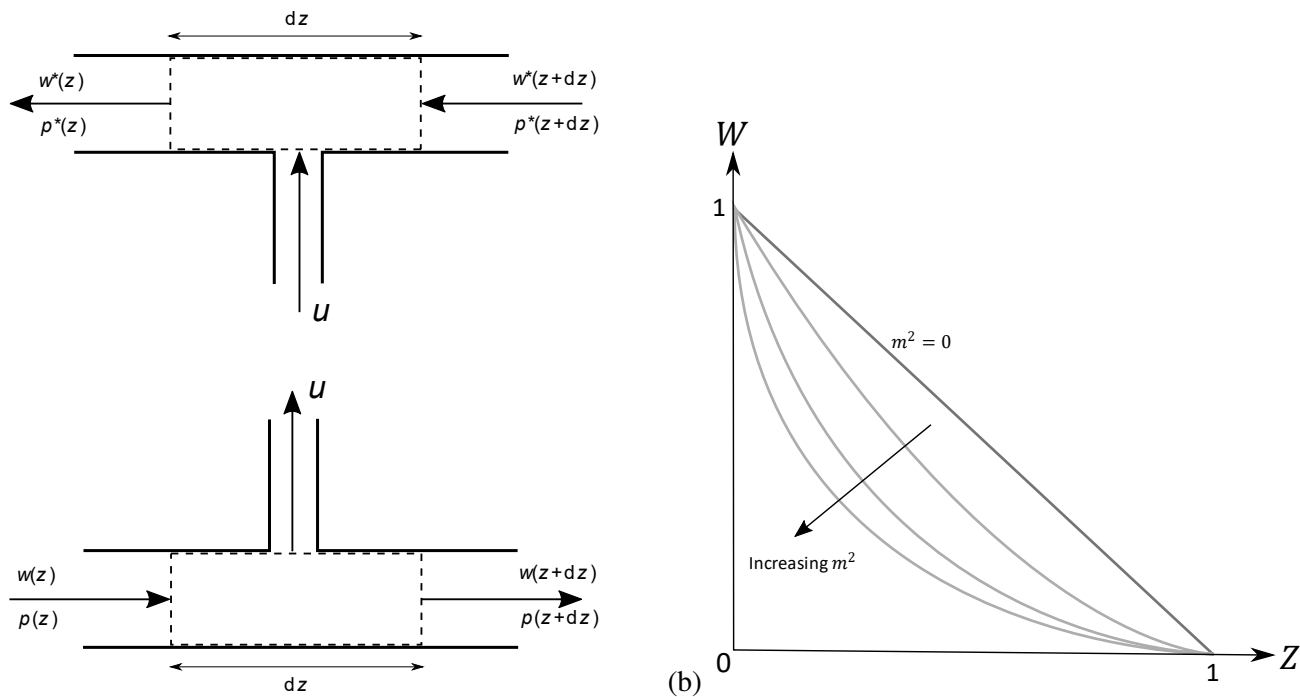


Figure 2.a) A schematic representation of the control volumes used in the derivation of the maldistribution model. The feed (left) and exhaust (right) manifolds are shown. Based on a schematic from Bassiouny and Martin [20] b) A graphical representation of how the dimensionless axial manifold velocity (w) is affected by the maldistribution number, m . The boundary conditions are $w(z=0) = 1$ and $w(z=1) = 0$ for the inlet manifold velocity and zero flow at the end of the manifold, respectively. The channel velocity for a given value of z is proportional to the negative of the gradient of the curve.

2.3. Limiting Current Density Model

The limiting current density is an important operational parameter in ED as it represents a practical upper bound for ion flux. Transport is fastest in the membranes and is significantly slower in diffusional boundary layers. Consequently, ion depletion and accumulation occurs at the diluting and concentrating sides of the membrane, respectively (Figure 1c) [23]. Concentration gradients resultantly form adjacent to the membrane surfaces through a phenomenon known as concentration polarisation. As the current density is increased, concentration polarisation is exacerbated and the diluate interfacial concentration decreases until it vanishes. This point is referred to as the LCD and coincides with a steep increase in electrical resistance. A further increase in the current density would initiate water splitting, leading to wasted energy, unwanted pH changes of streams, and in the most severe cases, membrane damage. It is therefore desirable to operate below the LCD; thus, the LCD is a key parameter for the design and operation of ED stacks. It is therefore crucial for the wider deployment of ED that the effect maldistribution has on LCD is evaluated.

This work utilises mass transfer coefficients and linear representations of diffusional boundary layers to compute an estimate for the LCD. It is assumed that the LCD will be reached at the point where the concentration in any channel vanishes [24] which will first occur at the exit of the slowest diluate channel since it has the greatest residence time. Assuming a constant flux over the entire membrane (suitable for short stacks with a low residence time), the LCD may be calculated by the following equation.

$$\hat{i} = \frac{F}{\phi} \frac{C_i u_{10} \beta}{\sqrt{u_{10} d} + \beta \frac{L}{d}} \quad (16)$$

241 Here, \hat{i} is the LCD, ϕ is the current efficiency, F is the Faraday constant, C_i is the inlet concentration, u_{10} is the
 242 velocity of the slowest channel, d is the intermembrane spacing, L is the channel length, and β is a dimensionless
 243 parameter of physical properties. The value of β is determined as follows.

$$\beta \equiv \frac{0.29}{\sqrt{2}} \sqrt[6]{\rho/\mu} D^{\frac{2}{3}} \quad (17)$$

244 The value of u_{10} may be determined using Eq. (15), setting the value of Z/L equal to unity.

$$u_{10} = \left(W_0 \frac{A_m}{n A_c} \right) \frac{m}{\sinh m} \quad (18)$$

245 Therefore, this is a model that can estimate the LCD as a function of the maldistribution number, m . The full
 246 derivation of this model may be found in the electronic supplementary information file (Section S1). Eqs. (16) and
 247 (18) were solved directly in MATLAB R2020b for a range of m between 0 and 6 for the nominal geometry and inlet
 248 flowrate defined in Table 1.

249 2.4. Resistance Model

250 The overall stack resistance is an important consideration as it directly impacts both the operating cost through the
 251 energy consumption and the capital cost through overall membrane area required. It is therefore important to
 252 investigate how the stack resistance changes with the degree of maldistribution. Ohm's law shows how, for a given
 253 overall charge transfer rate (*i.e.*, current, often process fixed), a higher resistance (R in [$\Omega \text{ m}^2$]) must lead to either a
 254 higher voltage (V), or greater membrane area (A).

$$\text{Charge transfer rate} = iA = VA/R \quad (19)$$

255 Voltage is the work done per unit charge, and so is proportional to the specific energy consumption of separation.
 256 Hence, an increase in resistance will ultimately lead to an increase in either the capital costs through greater
 257 membrane requirements, or operating costs through a greater energy consumption.

258 To evaluate the stack resistance, a circuit-based model is used. Differential mass balances are used to evaluate the
 259 evolution of the concentration inside the channels.

$$\frac{dC}{dx} = -\frac{1}{u d} \dot{N} \quad (20)$$

260 The stack is imagined as a set of resistors in series, the total resistance of which is used to relate variables such as the
 261 voltage and current density to the ion flux through Ohm's law and Faraday's law. These resistors correspond to the

262 membrane, the bulk electrolytes (diluate and concentrate) and the diffusional boundary layers. Membrane resistance
263 is assumed to be constant. The electrolyte resistance is calculated from the conductivity which in term is assumed to
264 be directly proportional to the electrolyte concentration. A more detailed description of this model can be found in
265 the ESI (section S2). In this model, it is assumed that the cell voltage (V_{cell}) is fixed at 1.2 V.

266 This system of algebraic and differential equation was solved in MATLAB R2020b using the function ode45. Sodium
267 bicarbonate was used as the species of study, specified by using value of $13.6 \text{ mS cm}^{-1} (\text{mol/m}^3)^{-1}$ for the molar
268 conductivity. It should be noted that very similar results may be obtained with alternate species, specified through
269 using the appropriate value of the molar conductivity.

270 3. Results – Quantifying Maldistribution

271 This section explores and quantifies the extent of inhomogeneous flow distribution observed in the simulated flow
272 profiles. Maldistribution results are presented in graphs of channel number *versus* channel velocity. A numbering
273 convention is taken here representing the channel’s distance from the inlet and outlet ports. ‘Channel n ’ is the n th
274 closest to the inlet, with channel 1 being the closest. The points on the distribution profile graphs (typically part b in
275 figures) represent the magnitude of the centreline velocity averaged over several points (shown in Figure 1d),
276 simulated in Fluent. Unless otherwise stated, the lines represent the maldistribution model (Eqs. 4 and 5) fit to the
277 Fluent distribution using the MATLAB function lsqnonlin.

278 3.1. Maldistribution Model Validation

279 To determine the applicability of the maldistribution model derived for a PFHEX to that of ED, it was compared to
280 a standard-case simulation using the nominal conditions described in Table 1. This simulation was also used to
281 confirm the existence of maldistribution in typical ED systems.

282 A value for the maldistribution number, m , was determined in two different ways: calculation using channel data and
283 Eqs. (7) and (8), and by fitting the model (Eq. (15)) directly to the flow distribution profile (Figure 3a). This was
284 done to evaluate both the applicability of the model and how representative the calculated value of m is. To calculate
285 m , values for ΔP_{mc} and U_{mc} were computed directly from the Fluent simulation results and subsequently used to find
286 m to be 1.30. To fit the maldistribution model (Eq. (15)) to the velocity distribution, a MATLAB non-linear least-
287 squares fitting tool (lsqnonlin) was used to find optimum values of W_0 and m . These were determined to be $m =$
288 1.33 and $W_0 = 0.157 \text{ m/s}$. The closeness of the fitted and calculated values (Table 2) shows that Eq. (7) is a good

289 representation of the maldistribution number for ED. It also shows, for the first time, that this model is a powerful
290 tool for predicting the distribution of flow in an ED stack.

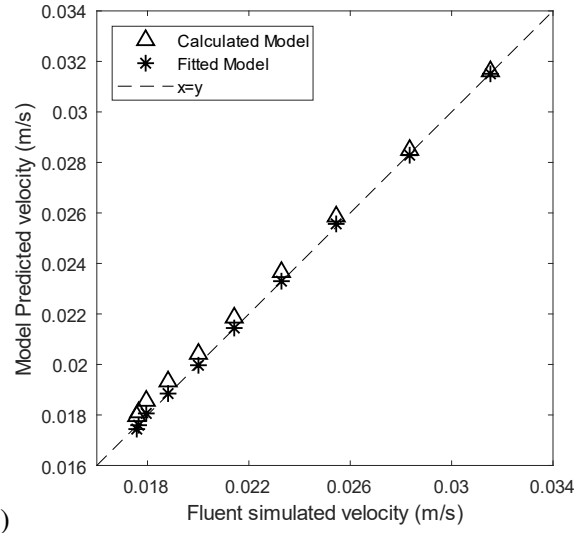
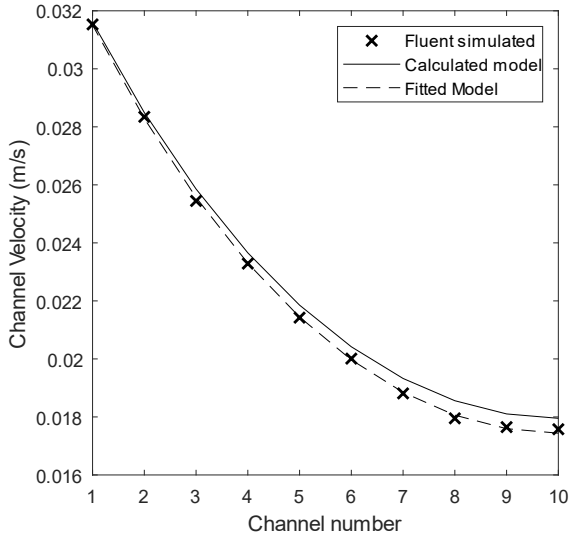
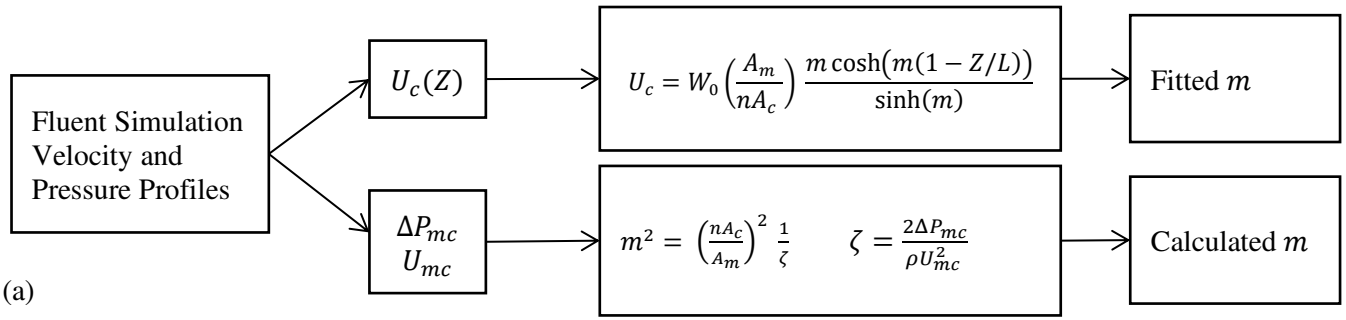
291 The simulated flow profile reveals that the velocity is greatest in channel one and decreases in each subsequent
292 channel at a decreasing rate (Figure 3b). Significant maldistribution is seen, with the greatest channel velocity nearly
293 twice that of the slowest. Channel one will therefore have just over half the residence time of channel ten, and so the
294 performance between channels will vary significantly. It can therefore be concluded that maldistribution is significant
295 in the simulated standard ED stack under reasonable operating conditions with a flow rate of 45 L/h (average of 4.5
296 L/h per channel).

297 Maldistribution is pronounced because there is a higher flow rate in the manifolds nearer to the stack entrance and
298 exit. The flow rate subsequently decreases along the manifold (and the z-coordinate) as fluid is distributed to the
299 channels. Therefore, a greater momentum is transferred to lower numbered channels and the flow takes the path of
300 least resistance.

301 For the model using the calculated value of m , a better fit is seen for lower numbered channels with higher flow rates
302 (Figure 3c), with the model over-predicting high-channel velocities. This could be partly due to the assumption of
303 negligible wall friction. The effect would be small for channels close to the entrance but lead to a non-negligible
304 reduction in momentum for late channels.

305 Both the calculated and fitted models show good qualitative and quantitative agreement with the simulated data and
306 very low root-mean-square (rms) relative errors (Table 2). This gives confidence that the maldistribution model
307 provides an accurate representation of the overall flow distribution. Fitting of the model to the flow profiles gives an
308 accurate representation of the flow distribution. Comparison of the trend in m to what is expected from Eqs. (7) and
309 (8) is useful in determining the underlying causes of these trends. This model will be used for quantification of
310 maldistribution in simulations and used to recreate flow profiles for the LCD and resistance models below.

311 For comparison, Kumar and Singh [21] computed m to be 0.54 for a PFHEX with 27 plates. It would be expected
312 that m would be significantly less for PFHEX than for ED due to the much larger manifolds used and thus much
313 greater value of A_m . However, a similar order of magnitude result gives further confidence in the applicability of this
314 result.



317 *Figure 3. a) A flow chart showing the process through which the calculated and fitted values of the maldistribution number are determined using Fluent*
 318 *simulation data. b) The distribution of velocity between the ten channels of the standard-case stack with the calculated model (Eq. (15)) and the fitted model*
 319 *predictions shown. Channels are numbered with one being the channel closest to the inlet and outlet, and ten being the farthest. c) the model predicted velocity*
 320 *plotted against the fluent simulated velocity for both the calculated and fitted models.*

321 *Table 2. The calculated and fitted values for the maldistribution number (m) and inlet velocity (W_0), as well as the relative root mean square (rms) error*
 322 *between the maldistribution model and simulated velocities.*

	Calculated	Best-fit
m	1.30	1.33
W_0 (m/s)	0.159	0.157
rms relative error	2.1%	0.4%

325 3.2. Inlet Flow Rate

326 The inlet flow rate to the ED stack is an important parameter as it determines the total process throughput. For a
 327 given process, the overall throughput is typically fixed by other unit operations, and so instead can be altered by
 328 using multiple stacks in parallel and splitting the flow between them.

329 A stack with the standard geometry (Figure 1d) was simulated, and the manifold inlet velocity was varied between
 330 0.04 m/s and 0.32 m/s. It is shown in Figure 4 that increasing inlet flow rate increases the degree of flow
 331 maldistribution between channels. Higher flow rates can be seen to increase the value of m , but at a decreasing rate,
 332 and the distribution of velocity can be seen to broaden (Figure 4a). The velocity in individual channels appears to

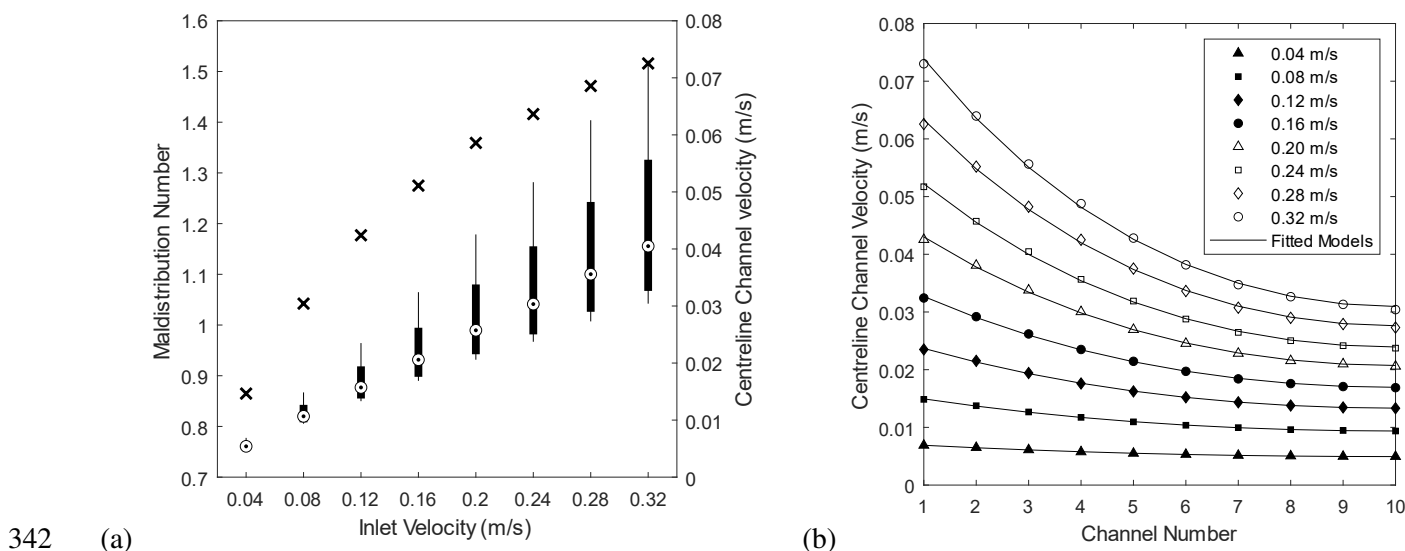
333 increase linearly (Figure 4b), suggesting that the velocity of each channel is proportional to the inlet flow rate. This
 334 agrees with what is predicted in Eq. (15).

335 The increase in maldistribution can be explained using the analytical model by combining Eqs. (7) and (8):

$$m \propto U_{mc} / \sqrt{\Delta P_{mc}} \quad (21)$$

336 The inlet flow rate is approximately proportional to the median channel velocity, U_{mc} . However, accompanying the
 337 increase in mean channel velocity is a non-linear increase in the channel pressure drop, resulting in a non-linear
 338 relationship between the inlet flow rate and maldistribution number.

339 The consequences of this are that the flow maldistribution may be significantly reduced by decreasing the inlet flow
 340 rate. Industrial scale stacks tend to have flow rates three orders of magnitude higher (10 – 100 m³/h), and so from
 341 this effect it would be expected that they would experience greater maldistribution.



343 *Figure 4.a) Fitted values of the maldistribution number (X, left y-axis) and a box-and-whisker diagram showing the distribution of the velocity across the*
 344 *stack (right y-axis) for simulations where the inlet velocity was changed. Targets (O) give the median velocity, boxes represent the interquartile range, and*
 345 *lines show the overall range of velocity. b) The distribution of flow between channels for a varying inlet flow rate with channel one being the closest to the*
 346 *stack inlet. Also shown is the fitted maldistribution model for each flow rate (Eq. (15)).*

347 3.3. Channel Width

348 A series of simulations were run where the width of the channel was varied between 0.2 mm and 1.8 mm to determine
 349 the effect of this geometric parameter on maldistribution. The manifold inlet flow rate was maintained at 45 L/h, and
 350 so the velocity in each channel should increase as the intermembrane distance decreases. The intermembrane distance
 351 determines the channel width and is directly controlled by the geometry of the spacer. Both bench-scale and
 352 industrial-scale stacks tend to have a very thin channels on the order of 1 mm. This is because the electrolyte
 353 resistance is proportional to its length in the direction of the electric field. Hence, thinner channels should
 354 theoretically have lower electrical resistances, all else being equal. Thinner channels do, however, have a higher flow

355 resistance, requiring greater pumping power and increasing the risk of solution leakage. Further, the risk that
356 membranes will touch and short-circuit is increased.

357 Increasing the channel width increases the degree of maldistribution (Figure 5). Wider channels have a lower velocity
358 since inlet flow rate is held constant. A greater maldistribution is seen from the broader distribution of velocities
359 between channels. This is confirmed by the trend in m which increases substantially as channel width is increased.
360 The 0.2 mm thick channel experienced very little maldistribution and with a value of m of only 0.10, but this
361 increased to 2.44 as the channel width is increased to a maximum of 1.8 mm.

362 The relationship between m and channel width appears to be near-linear with only slight convex curvature over the
363 range studied. A proportional relationship would be expected from Eq. (7) since

$$A_c = d \times w_m \quad (22)$$

364 For this to hold, the friction coefficient must be constant. For laminar flow, the friction coefficient is found from the
365 Reynolds number correlation for the Darcy friction factor as a consequence of Poiseuille's Law:

$$f_d = 64/Re \quad (23)$$

$$\zeta = f_d \cdot \frac{L}{d_h} = \frac{64}{Re} \cdot \frac{L}{d_h} \quad (24)$$

366 The mean channel Reynolds number is proportional to the product of the velocity and the channel width (assuming
367 d_h is twice the intermembrane space).

$$Re \propto u \cdot d \quad (25)$$

368 The channel volumetric flowrate, Q_c is held constant and is the product of u and A_c . Therefore, the Reynolds number
369 is expected to be constant

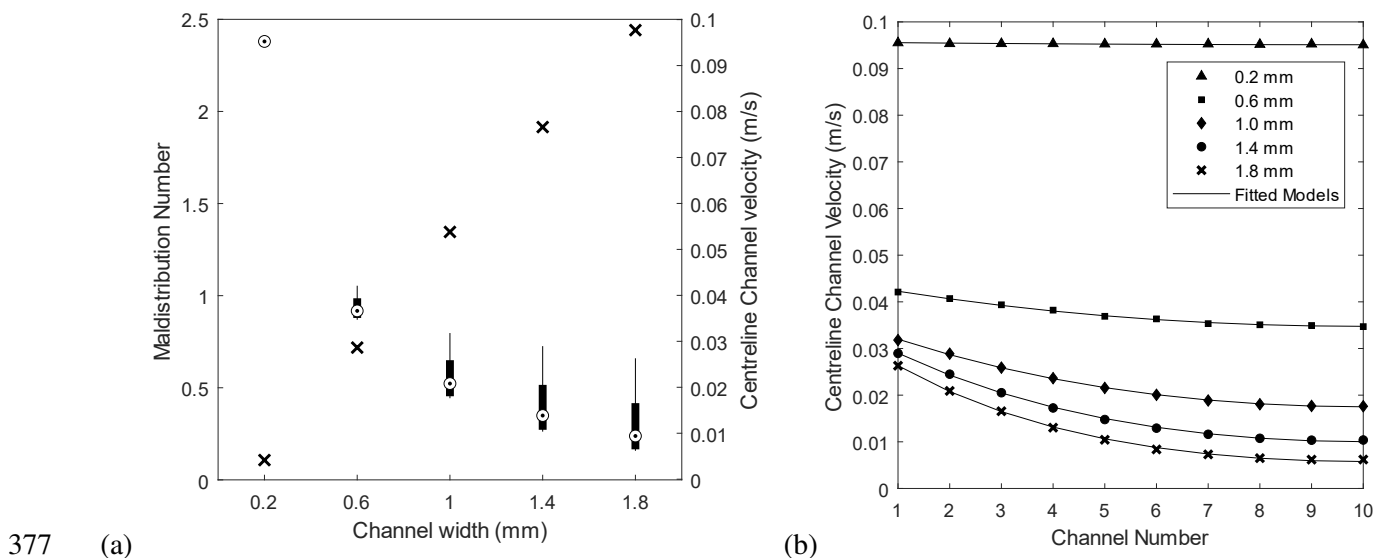
$$Re \propto Q_c/w_m \quad (26)$$

370 Thus, if laminar Poiseuille flow is assumed, the friction coefficient would be expected to be inversely proportional
371 to d_h (Eq. 24). This would result in m having the following relationship with d_h

$$m \propto d_h^{3/2} \quad (27)$$

372 and Figure 5a showing a non-linear trend, which is not the case. It can therefore be concluded that the fluid dynamics
373 deviates significantly from ideal Poiseuille flow, with phenomena such as entrance effects having a significant effect.

374 It has been shown by the results that a reduction in the channel width can reduce the degree of maldistribution. This
 375 would, of course, contend with other factors such as the pressure drop which would affect the mechanical stability,
 376 pumping power, and solution leakage.



377 (a) 378 *Figure 5. a) Fitted values of the maldistribution number (X, left y-axis) and a box-and-whisker diagram showing the distribution of the velocity across the*
 379 *stack (right y-axis) for simulations where the channel width was changed. Targets (O) give the median velocity, boxes represent the interquartile range, and*
 380 *lines show the overall range of velocity. b) The distribution of flow between channels for a varying channel width with channel one being the closest to the*
 381 *stack inlet. Also shown is the fitted maldistribution model for each channel width (Eq. (15)).*

382 3.4. Distributor Angle

383 *The geometry of the distributor connecting the manifolds to the channels varies widely across ED applications. It is*
 384 *controlled by the spacer design, and so any feasible geometry can be easily created. This study looks at the effect of*
 385 *the distributor geometry on maldistribution by changing the angle the distributor makes with the horizontal manifold*
 386 *centreline. To do this, two points on the horizontal diameter of the manifold were set, each 0.5 mm away from the centre (*

387 Figure 6a). From these, two lines were drawn up to the channel with a specified angle made to the vertical. The angle
 388 recorded is that of intersection between the two lines, equivalent to twice the angle the lines make with the vertical.
 389 All other aspects of the geometry were maintained at the nominal values, and the inlet flow rate was held at 45 L/h.

390 *It is suggested by the results that wider distributors, with a larger angle, lead to greater maldistribution. Profiles from*
 391 *simulations with wider distributor angles have a broader velocity distribution (*

392 Figure 6b & 6c). This observation is repeated in the trend of the maldistribution number, which shows a smooth
 393 curve with a positive but decreasing gradient. It is seen from the results that the increase in the maldistribution slows
 394 at higher angles. There is a difference in the value of m of 0.57 between the 0° and 45° simulations, but only 0.07
 395 between 135° and 180° .

396 The geometry of the distributor is not directly accounted for in the maldistribution model since a two-dimensional
397 approximation is taken in its derivation (Section 2.2). This is one of the key limitations of simulating ED in 2D as
398 the distributor geometry clearly has a significant effect on flow distribution. However, the effect on maldistribution
399 number is captured through the channel pressure drop. It can be seen from Eqs. (7) and (8) that m is inversely
400 proportional to the square root of the pressure drop.

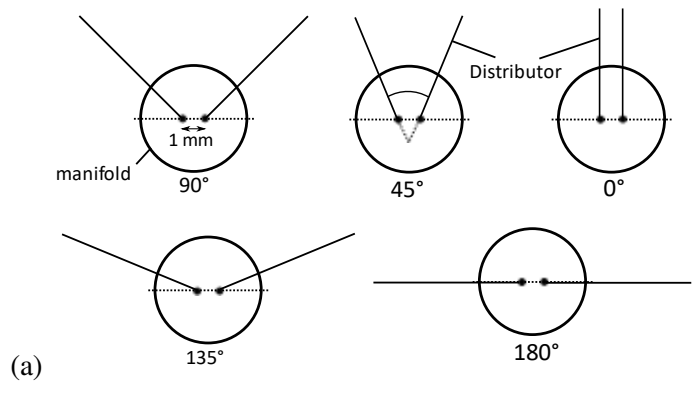
$$m \propto 1/\sqrt{\Delta P_{mc}} \quad (28)$$

401 Narrower distributors will have a larger associated pressure drop, and so would be expected to have less
402 maldistribution. A physical interpretation of this is that due to the higher pressure drop of the distributor, a lower
403 proportion of the manifold flow momentum is transferred to the channels nearer the entrance and exit, and so the
404 fluid is distributed more uniformly. The flow is essentially held back in the manifold due to the restrictive distributor.
405 The consequence of this is that maldistribution may be reduced by changing the spacer geometry to have narrower
406 distributors. However, this also comes with an increase pressure drop and thus increased pumping power and greater
407 solution leakage between channels. Spacers used at both the bench and industrial scales have very varied geometries
408 from narrow groves in the spacer to wide-open distributors. Therefore, this may be an important lever when it comes
409 to reducing maldistribution. This may also present a potential solution to maldistribution in ED. The angle of the
410 distributor be increased in subsequent channels to artificially restrict flow in early channels and manipulate individual
411 pressure drops. This may be tuned to counteract the effect of a higher manifold flowrate in early channels. The exact
412 nature of this solution is, however, not trivial to determine, and would lead to an overall increase in the pressure drop.
413 The latter increases the pumping power required, and the probability of solution leakage.

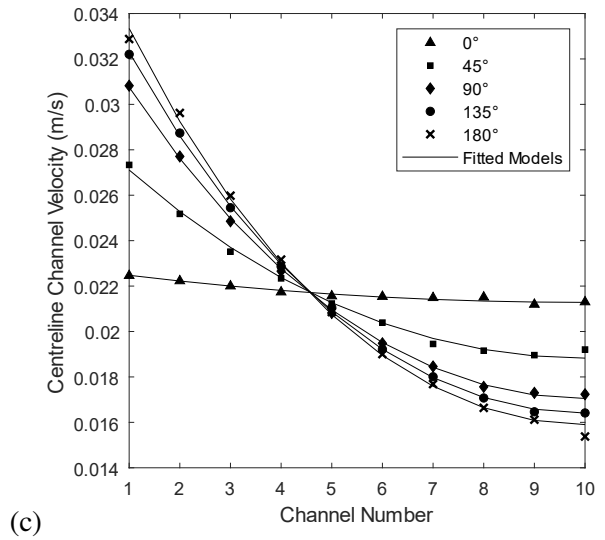
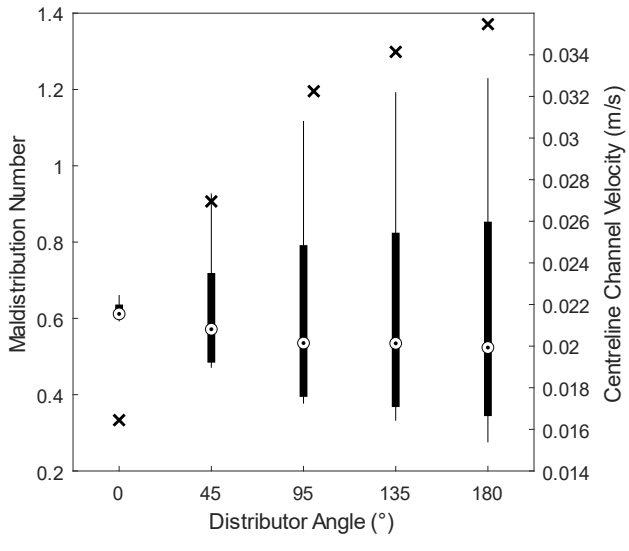
414

An additional important caveat to reducing distributor angle is the appearance of jetting effects at the channel inlet (
415 *Figure 6d). They arise due to the increased velocity present in the distributor because of the reduced flow area, and*
416 *lead to stagnant flow regions either side of the distributor. Ion depletion occurs rapidly in these stagnant zones, and*
417 *results in a reduction in the effective membrane area and other negative effects of operating beyond the limiting*
418 *current density (pH changes, wasted energy and potential membrane damage from an extreme pH).*

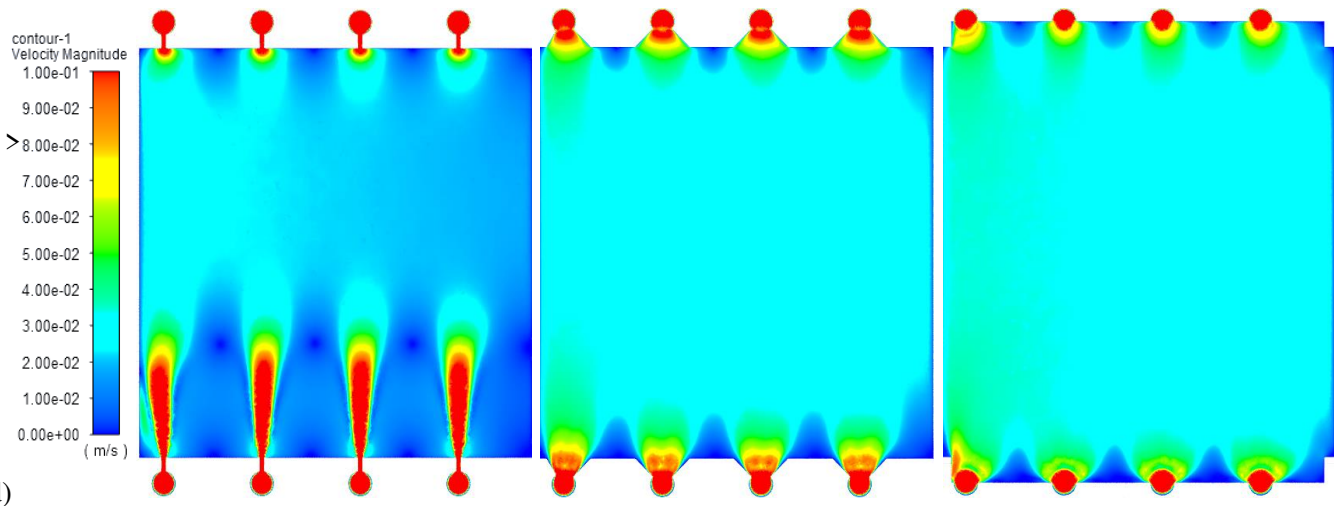
419



420



421



422

423 Figure 6. a) A schematic representation of the distributor geometry and how the angle is defined. b) Fitted values of the maldistribution number (x, left y-axis)
 424 and a box-and-whisker diagram showing the distribution of the velocity across the stack (right y-axis) for simulations where the distributor angle was
 425 changed. Targets (o) give the median velocity, boxes represent the interquartile range, and lines show the overall range of velocity. c) The distribution of flow
 426 between channels for a varying distributor angle, with channel one being the closest to the stack inlet. Also shown is the fitted maldistribution model for each
 427 distributor angle (Eq. (15)). d) A contour plot showing the centreline velocity profile in the fastest channel for three distributor angles, 0°, 90° and 180° from
 428 left to right

429

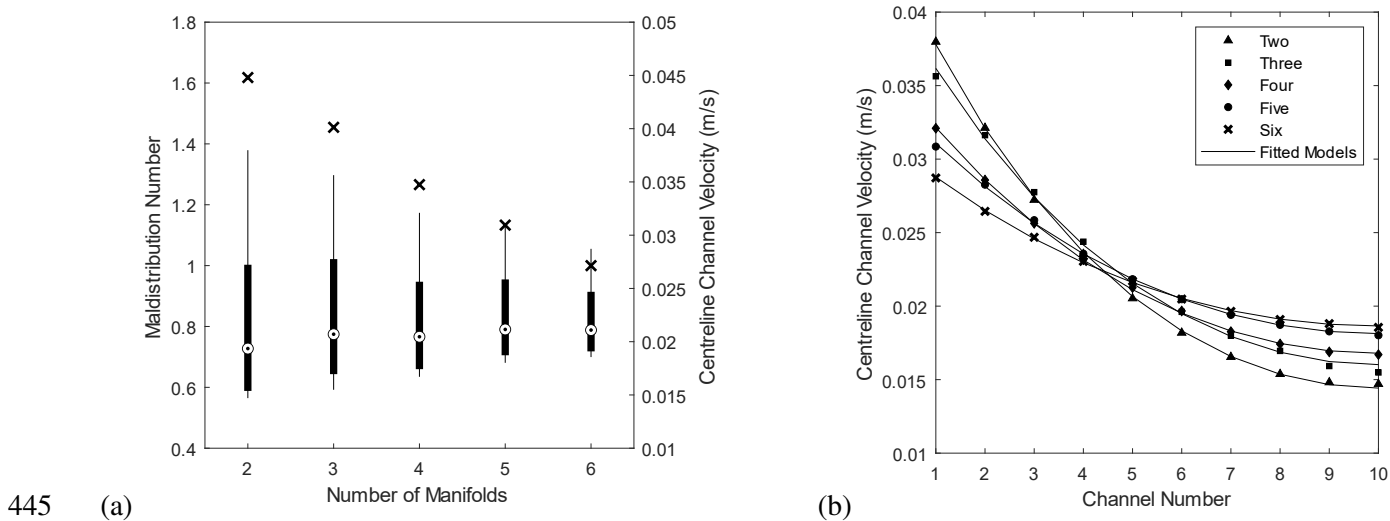
3.5. Number of Manifolds

430 The number of manifolds in a bench-scale stack is typically between four and six, but it is common for large-scale
 431 instillations to have only one. The number of manifolds is built into the stack design, and so is not as easily

432 manipulated in practice as other parameters. These simulations were run by changing the geometry of the simulated
 433 stack to increase the number of equally spaced manifolds and reducing their spacing. The manifolds were moved off-
 434 centre, so that if the manifolds of the other stream were present, the stack would be symmetrical. The inlet velocity
 435 was subsequently scaled to maintain the same overall flow rate to the stack. All other parameters including the
 436 distributor geometry and channel width remained unchanged.

437 It is shown by the results that a greater number of manifolds leads to a lower degree of maldistribution (Figure 7).
 438 Increasing the number of manifolds from two to six reduces the maldistribution number from 1.62 to 1.00. This is
 439 expected from the maldistribution model (Eq. (7)), where m is inversely proportional to the manifold area.

440 An explanation for why maldistribution worsens with a lower number of manifolds is due to the higher velocity
 441 present in the manifold. The manifold inlet flow rate is constant, so reducing the manifold area leads to an increase
 442 in the velocity. Similar to the case of increasing flow rate (Section 3.2), the fluid in the manifolds has a higher
 443 momentum, and so will transfer a greater proportion of it to the channels nearer the entrance, with less left over for
 444 those farther away.



446 *Figure 7. a) Fitted values of the maldistribution number (✕, left y-axis) and a box-and-whisker diagram showing the distribution of the velocity across the*
 447 *stack (right y-axis) for simulations where the number of manifolds is changed. Targets (⊙) give the median velocity, boxes represent the interquartile range,*
 448 *and lines show the overall range of velocity. b) The distribution of flow between channels for a varying number of manifolds, with channel one being the*
 449 *closest to the stack inlet. Also shown is the fitted maldistribution model for each case (Eq. (15)).*

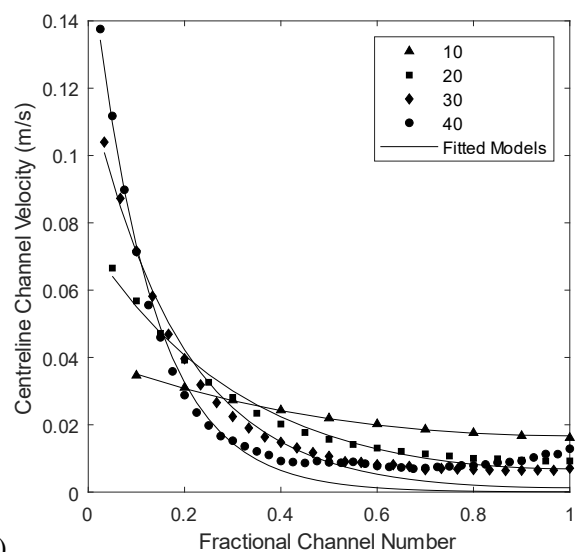
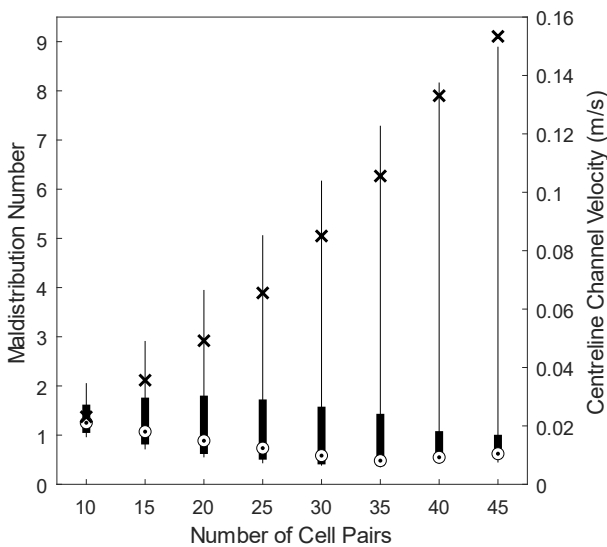
450 3.6. Number of Cell Pairs

451 A repetitive geometry is one of the key strengths of ED, making it modular and easily scalable. It allows for relatively
 452 consistent designs of stacks to be used for different throughputs, with the number of cell pairs being scaled to maintain
 453 a consistent residence time. Bench-scale stacks tend to use between ten and twenty cell pairs, whereas pilot-scale can
 454 reach 50, and industrial-scale can be over 200 pairs.

455 A set of simulations was carried out, varying the number of flow channels between 10 and 45. Attempts at simulations
 456 with a greater number of cell pairs failed to converge, presumably due to the high velocity gradients in manifold-
 457 channel junctions close to the entrance and exit. It was revealed by the simulations that increasing the number of cell
 458 pairs significantly increased maldistribution (Figure 8a). The value of m ranged from ~ 1 when ten cell pairs were
 459 used, to more than 9 with 45 cell pairs. The effect of the number of cell pairs on maldistribution was significantly
 460 more than any other parameter investigated.

461 It is indicated by Eq. (7) that m is directly proportional to the number of cell pairs, and so the trend observed in Figure
 462 8a is expected. The strong dependence of m on the number of cell pairs is notable due to the very high number used
 463 at an industrial scale. Maldistribution is expected to be worse when more cell pairs are used, and so this shows the
 464 importance of leveraging the other parameters mentioned to prevent it becoming unmanageable.

465 A caveat is revealed by these results; the goodness of fit of the model is reduced for simulations of a high number of
 466 cell pairs in the slower channels (Figure 8b). The maldistribution model predicts that the velocity should tend to zero
 467 in this case, but the Fluent model shows that instead a steady value of around 0.01 m/s is reached, or that the velocity
 468 increases in further channels. Therefore, there is inaccuracy in either the Fluent simulation or the maldistribution
 469 model. Simulating a high number of cell pairs in Fluent is very computationally demanding, as the volume of the
 470 domain increases, and denser meshes are required around junctions to account for the very steep velocity gradients
 471 between early channels and the manifolds. The total number of mesh cells therefore increases at an increasing rate.
 472 The velocity profile can be seen to oscillate slightly, indicating numerical instabilities. Additionally, the validity of
 473 the assumption of negligible wall friction would decrease as a higher number of cell pairs are considered.



474 (a)

(b)

475
476
477
478

Figure 8. a) Fitted values of the maldistribution number (\times , left y-axis) and a box-and-whisker diagram showing the distribution of the velocity across the stack (right y-axis) for simulations where the simulated number of cell pairs was changed. Targets (\odot) give the median velocity, boxes represent the interquartile range, and lines show the overall range of velocity. b) The distribution of flow between channels for a varying number of cell pairs with channel one being the closest to the stack inlet. Also shown is the fitted maldistribution model for case (Eq. (15)).

479

3.7. Length-to-Width Ratio

480

All previous simulations were carried out on an L/D of 1 since this is typical for lab-scale stacks. However, pilot and industrial stacks typically have an L/D of 2 to increase channel residence time and reduce the impact of localised effects such as stagnant regions. A comparative flow simulation was conducted on two stacks, identical except for one having double the channel length (16 cm) of the other.

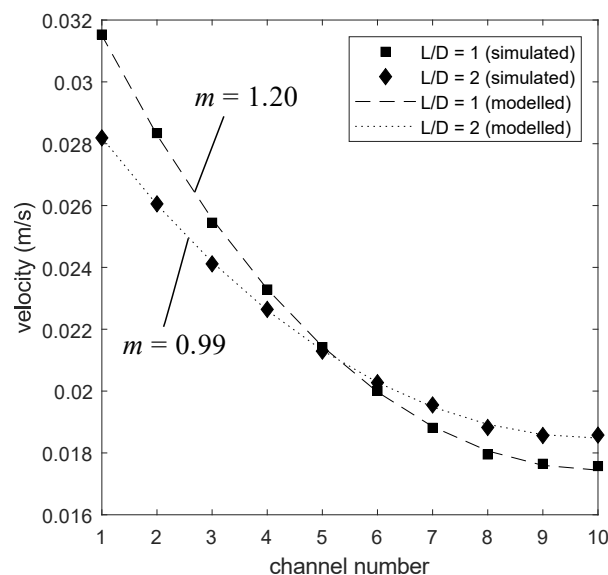
484

It is shown by the results that the maldistribution is slightly less for the longer flow path (Figure 9), with an L/D of 1 and 2 resulting in a maldistribution number of 1.20 and 0.99, respectively. The reasoning of this is the same as that of the distributor angle, where longer flow paths lead to higher pressure drops and thus a lower proportion of the momentum of the manifold flow is transferred to the channel.

488

As a result, the higher L/D used at industrial scale would go some way to reducing the maldistribution, but the effect is relatively low compared to other parameters studied. A similar effect would be expected from the presence of a netted spacer, which can, on average, increase the pressure drop by about 55% [29]. Eq. (28) shows how m is inversely proportional to the square root of the mean channel pressure drop. It can therefore be estimated that the presence of a spacer would reduce the value of m by about 20%.

492



493

494
495

Figure 9. The velocity distribution for simulations where the length-to-width ratio (L/D) was changed. The simulated velocities are shown as points. Also displayed are the results of the fitted maldistribution model, shown as lines.

4. Consequences of Maldistribution

It has been shown in Section 3 that maldistribution exists in ED and that it is affected by stack geometry and inlet flow rate. It can be shown from the maldistribution model that the ratio of the velocity of the fastest channel to the slowest channel is $\cosh m$. A value of m of 1.3, which could be considered moderate, would lead to twice the flowrate through the fastest channel compared to the slowest, and thus the fluid would have half the residence time. Understanding the effect this has on ED operation is vital as it raises the question ‘to what degree maldistribution is an issue that needs addressing?’ It is expected that performance decreases as maldistribution worsens; this section investigates to what degree this is true. Two operational metrics were chosen for this investigation, the LCD and stack resistance, as these represent local and global effects, respectively.

4.1. Limiting Current Density

The LCD is a practicable upper bound for ion flux, and thus reductions in LCD are detrimental for process intensification purposes. The one-dimensional model outlined in section 2.3 was used to determine the change in LCD with maldistribution. It is clear from the results that the limiting current density decreases significantly as maldistribution worsens (Figure 10a). The LCD as a function of m is plotted, where the LCD has been scaled to a case of uniform flow distribution ($m = 0$). This non-dimensionalisation was done to remove the effects of variables such as the inlet concentration, channel residence time, and current efficiency. Hence, the y-axis represents the LCD as a fraction of that for a uniformly distributed case. As m increases, the scaled LCD rapidly drops before asymptotically approaching zero. An inflection point is seen at $m = 1.63$, where the LCD has fallen to 67% of the uniform distribution value.

The reason LCD decreases as maldistribution worsens is because it is reached first when the membrane-electrolyte interfacial concentration for the slowest channel vanishes. Concentration polarisation is always greatest at the end of the slowest diluting channel, since it has the longest residence time, and thus the greatest amount of salt removed. As m increases, the velocity in the slowest channel decreases, the residence time increases, and hence the outlet concentration decreases. Therefore, a zero interfacial concentration is reached with a lower flux, and the LCD is lower. It can be seen from Eq. (18) that the velocity of the slowest channel decreases as m increases.

$$u_{10} \propto \frac{m}{\sinh m} \quad (29)$$

521 The $\sinh m$ term grows much faster than m , leading to an overall decrease in the slowest channel velocity which
522 tends to zero as m gets large. This is expected from the broadening of the velocity distribution. The residence time
523 subsequently increases and so a lower flux is needed to achieve a zero interfacial concentration.

524 The magnitude of the reduction in LCD resulting from maldistribution is large, with a ‘moderate’ maldistribution of
525 $m = 1.3$ leading to a 23% reduction in the LCD. This has significant consequences for process intensification.
526 Generally, it is desirable to operate just below the LCD since a higher current density results in a higher ion flux.
527 There is a subsequent reduction in required membrane area and unit size, leading to lower costs. A reasonable increase
528 in maldistribution leads to a marked reduction in the LCD, significantly hindering performance.

529 The effect that maldistribution has on LCD is not one that has been studied much before, despite its apparent
530 prevalence. Tanka [25,26] modelled how the LCD decreased as the standard deviation of the stack velocity increased.
531 It was assumed that the slowest flow path has a velocity three standard deviations below the mean. While this was
532 useful to show the effects of maldistribution, the velocity distribution in a stack is far from normal, and so the
533 application of a dimensionless maldistribution number gives a more realistic depiction.

534 It is suspected that the lack of research into maldistribution in published literature may be because of the large number
535 of confounding variables in ED. The LCD is typically accounted for in both modelling and experimental papers as
536 an empirical power law, with the inlet concentration and occasionally the velocity as variables. All contributing
537 phenomena to the LCD are therefore lumped into a single model, the effects of which are subsequently obscured.
538 Many phenomena that are difficult to quantify have been identified as leading to a reduced LCD including solution
539 leakage [29] and ionic shortcuts [30]. The degree of turbulence in the channel also significantly affects the thickness
540 of the laminar boundary layers, which alters the LCD in a non-linear way. It is therefore reasonable that
541 maldistribution and its effects have gone unnoticed, as it is challenging to measure experimentally, and its effects
542 may be obscured by many confounding variables.

543 4.2. Stack Resistance

544 The stack electrical resistance is important to the overall performance of ED. An increase in resistance will lead to
545 an increased cost either in terms of a greater required membrane area or higher voltage to achieve the same charge
546 transfer rate (Eq. (19)).

547 Figure 10b shows the scaled resistance as a function of m for a series of different inlet concentrations. Like the
548 analysis performed for the LCD (Figure 10a), the y-axis gives the ratio of the resistance to a case of uniform flow
549 distribution ($m = 0$). This is again to remove the effect of confounding variables. Maldistribution leads to an increase

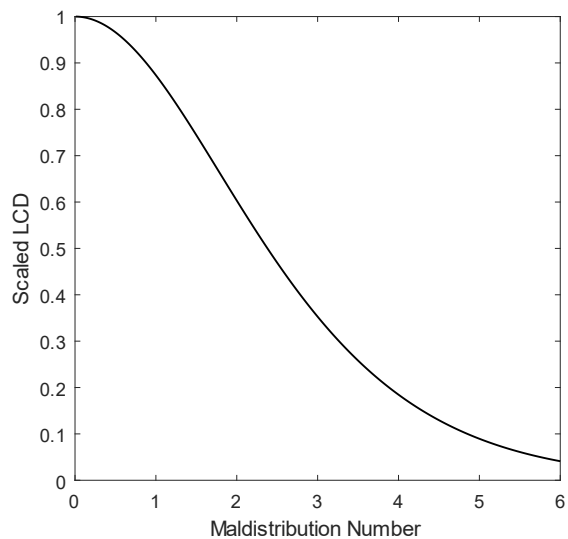
550 in overall resistance, which grows rapidly as m is increased. It can also be seen that the increase in resistance is
551 greater for lower inlet concentrations. The effect on resistance is less severe than the effect on LCD. A moderate
552 maldistribution with $m = 1.3$ has a 23% reduction in the LCD, however experiences only a 2% increase in overall
553 stack resistance for a 50 mol/m^3 inlet concentration.

554 Figure 10 c and d show the corresponding velocity and channel resistance profiles, respectively. It is shown by these
555 figures that the lower the channel velocity, the higher the resistance. The electrolyte resistance is inversely
556 proportional to concentration, and so a reduction in average channel concentration from a longer residence time leads
557 to a large increase in absolute resistance. Due to the reciprocal nature of the relationship, the effect of decreasing
558 concentration has a larger relative effect than increasing it. Hence, higher numbered channels are seen to deviate in
559 resistance more from the uniformly distributed case, and so the sum of the channel resistances is higher. When m is
560 increased, the velocity distribution broadens, and so the resistance distribution broadens also. These two effects
561 combined show why resistance increases with maldistribution. The greater increase in resistance for lower inlet
562 concentrations is also because electrolyte resistance is inversely proportional to concentration. The same absolute
563 change at a lower concentration has a much greater proportional effect.

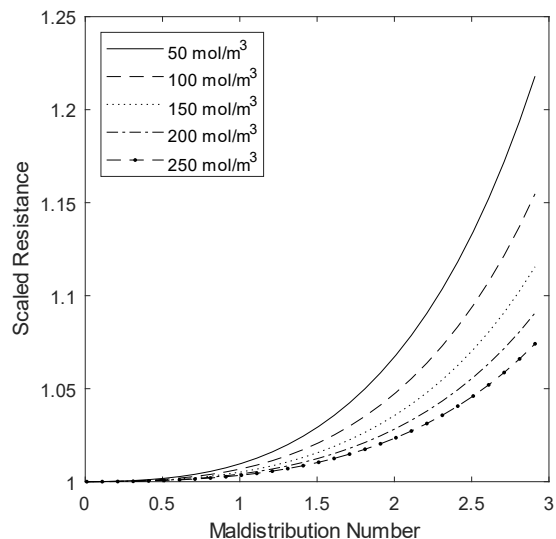
564 The effect on resistance is less severe than the effect on LCD because resistance is global whereas LCD is local. The
565 channels slower than the average lead to increase in resistance, but this is partly counteracted by the faster channels
566 having lower resistances. The slowest channel in the case where $m = 3$ (severe maldistribution) has about 70%
567 higher resistance than the average channel (Figure 10c & 10d), but the faster channels balance this out and lead to an
568 overall increase in resistance of only 20%. The effect on LCD only considers the slowest channel and so the effects
569 will always be more extreme. In the given case of $m = 3$, the LCD is reduced by about 75%.

570 This highlights that the effects of maldistribution may be more of a localised problem than a global one. It also further
571 explains why ED maldistribution has not had much attention historically. The issues of lower LCD and increased
572 localised concentration polarisation can be explained by many confounding phenomena and obscured in empirical
573 modelling. Whereas a significant increase in resistance is one that is less likely to go unnoticed.

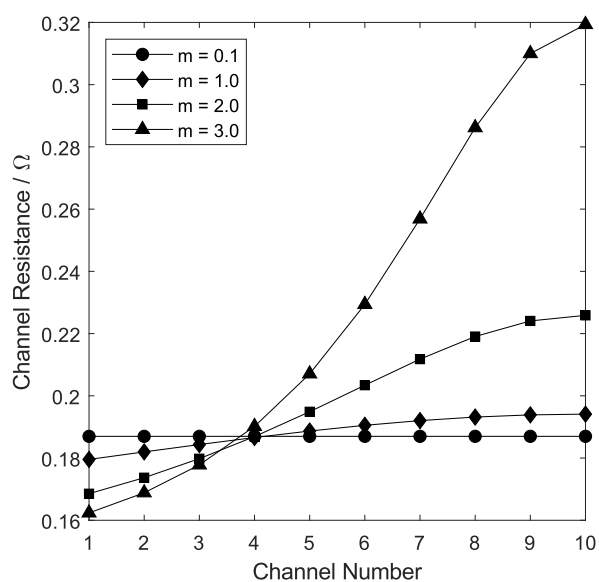
574 One caveat with the resistance model is that although it accounts for concentration polarisation, there is no
575 consideration for the LCD or associated phenomena such as water-splitting. As a result, as interfacial concentrations
576 approach zero, boundary resistances blow-up to infinity. The resistance would significantly increase only until water-
577 splitting occurs. It is therefore implicitly assumed that these simulations occur below the LCD.



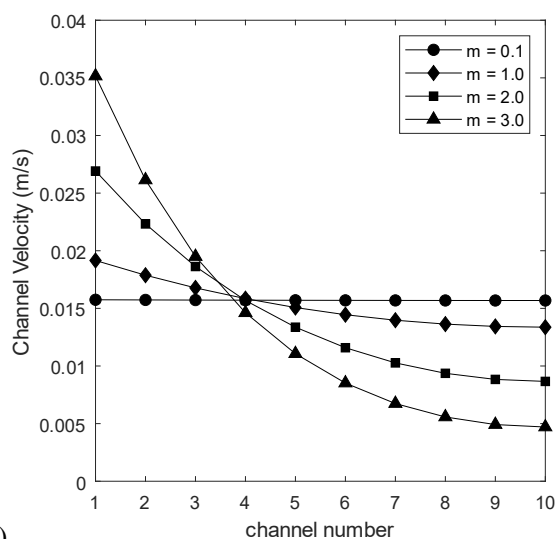
(a)



(b)



(c)



(d)

580 Figure 10. a) A graph of the scaled limiting current density (LCD) as a function of the maldistribution number. The LCD is normalised to a case of uniform
 581 flow distribution ($m = 0$) to remove the effects of confounding variable such as inlet concentration and current efficiency. b) The calculated resistance of a
 582 multi-channelled one-dimensional stack as a function of the maldistribution number for different inlet concentrations. The resistance is normalised to a case of
 583 uniform distribution ($m = 0$). c) The profile of channel resistance for different values of the maldistribution number. d) the velocity profile for different values
 584 of the maldistribution number. Low numbered channels are closer to the entrance and exit of the stack.

585 5. Conclusion

586 Maldistribution in ED was investigated through CFD simulations of a stack with varying geometrical and operating
 587 parameters. It was determined that the distribution of flow between channels is far from uniform. Therefore, the
 588 ubiquitous assumption of channel uniformity in ED modelling has been shown to be inaccurate. Further, a rigorous
 589 analytical model was found to accurately capture the distribution of flow between channels and represent the degree
 590 of maldistribution using a dimensionless number, m . The strong physical basis of this model allowed for the
 591 clarification of observed trends in simulations and provided a useful metric of maldistribution for use in one-
 592 dimensional models.

593 The simulations revealed that changes which increased the manifold velocity (reducing the number of manifolds,
594 increasing the number of cell pairs, and increasing the inlet flow rate) increased maldistribution. This is because
595 channels nearer to the entrance are adjacent to a higher velocity in the manifold, and so a greater amount of
596 momentum is transferred to those channels. This increases the proportion of flow to the channels closer to the
597 entrance and subsequently reduces the channel velocity of those farther away. Additionally, alterations which
598 increase the channel pressure drop (reducing the width of the distributor, reducing the channel width, and increasing
599 the L/D ratio) were found to reduce maldistribution by encouraging flow to remain in the manifold. From these
600 conclusions, it can be extrapolated that maldistribution will likely worsen at larger scales due to the much higher
601 number of membranes and larger flow rates. However, this must be confirmed either experimentally or through
602 simulations due to the large number of confounding influences present. This shows that maldistribution in ED is
603 likely ubiquitous, and so this research is important for all applications.

604 The impact of maldistribution on ED operation was investigated through two performance parameters. The LCD was
605 chosen as a representation of localised effects, and the stack resistance to represent global impacts. The effect of
606 maldistribution, through m , on these parameters was determined using a one-dimensional model. The results showed
607 that although the resistance was increased slightly, the impact on the LCD was significant. The maldistribution of
608 the standard geometry led to a 23% reduction in LCD, relative to a case where no maldistribution is present. This
609 highlights that the issues caused by flow maldistribution manifest at a localised level rather than a global one. It
610 further shows that maldistribution is an important phenomenon which significantly reduces the performance of ED
611 by limiting process intensification.

612 Flow maldistribution in ED has not had particularly much attention because the most significant effects, on LCD,
613 can be obscured by modelling it empirically and the presence of many confounding variables. This study has shown
614 that maldistribution in ED exists and that its effects are significant. Maldistribution should therefore be investigated
615 further, both experimentally and computationally across many scales to fully explore its prevalence and effects.

Symbol	Meaning
A	Membrane area
A_c	Channel area
A_m	Manifold area
C	Concentration of ionic species
D	Manifold diameter
d	Intermembrane distance
d_h	Hydraulic diameter
D	Mass diffusivity
E_T	Dimensionless ratio of convection to electromigration
F	Faraday constant
f_d	Darcy friction factor
\mathbf{g}	Gravitational acceleration vector
i	Current density
\hat{i}	Limiting current density
k	Mass transfer coefficient
L	Channel length
m	The maldistribution number
m_κ	Molar conductivity
n	Number of channels
\dot{N}	Ion molar flux
P	Pressure
p	Dimensionless pressure
Re	Reynold's number
R	Electrical resistance
Sc	Schmidt number
Sh	Sherwood number
t	Time
u	Channel superficial velocity
U_c	Channel velocity
u_c	Dimensionless channel velocity
\mathbf{v}	Vector velocity
V	Cell voltage
W	Manifold axial velocity
w	Dimensionless axial velocity
w_m	Membrane Width
W_0	Manifold inlet velocity
x	Coordinate for channel flow direction
Z	Axial distance coordinate
z	Dimensionless axial coordinate
z_q	Ion charge number

Greek Symbol	Meaning
τ_w	Wall friction coefficient
Δ	Change
β	Physical property parameter
δ	Boundary layer thickness
ζ	Channel friction coefficient
κ	Conductivity

μ	Fluid dynamic viscosity
ρ	Fluid density
ϕ	Current efficiency

619

Subscript	Meaning
*	Referring to the exhaust manifold
<i>aem</i>	Anion exchange membrane domain
<i>b</i>	Referring to the turbulent mixed zone of the channel
<i>BL</i>	Referring to the boundary layer
<i>c</i>	Referring to the channel domain
<i>cem</i>	Cation exchange membrane domain
<i>con</i>	Concentrate domain
<i>cell</i>	Referring to a variable across one cell pair
<i>dil</i>	Diluate domain
<i>e</i>	exit
<i>i</i>	The interface between electrolyte and membrane
<i>mc</i>	Mean Channel
<i>min</i>	The minimum of a set
<i>w</i>	Wall Boundary
0	inlet
10	Referring to the slowest channel

620

Abbreviation	Meaning
AEM	Anion Exchange Membranes
CEM	Cation Exchange Membranes
CFD	Computational Fluid Dynamics
ED	Electrodialysis
IEM	Ion Exchange Membranes
LCD	Limiting Current Density
PFHEX	Plate-and-Frame Heat Exchanger
rms	Root Mean Square
RO	Reverse Osmosis
RTD	Residence Time Distribution

621

622

623 7. Acknowledgements

624 This work was supported by the Engineering and Physical Sciences Research Council (EPSRC) [grant number
625 EP/T517835/1]; Shell Global Solutions International B.V.; and Kyra Sedransk Campbell would like to acknowledge
626 her Royal Society - EPSRC Dorothy Hodgkin Research Fellowship (DH15004).

- 629 [1] S. Al-Amshawee, M.Y.B.M. Yunus, A.A.M. Azoddein, D.G. Hassell, I.H. Dakhil, H.A. Hasan,
630 Electrodeialysis desalination for water and wastewater: A review, *Chem. Eng. J.* 380 (2020) 122231.
631 <https://doi.org/10.1016/j.cej.2019.122231>.
- 632 [2] UNESCO, Valuing water - The United Nations World Water Development Report 2021, *Water Polit.* (2021)
633 206. <https://unesdoc.unesco.org/ark:/48223/pf0000375724> (accessed July 16, 2021).
- 634 [3] M.T. Demeuse, Production and applications of hollow fibers, *Handb. Text. Fibre Struct.* 2 (2009) 485–499.
635 <https://doi.org/10.1533/9781845697310.3.485>.
- 636 [4] V.A. Shaposhnik, K. Kesore, An early history of electrodeialysis with permselective membranes, *J. Memb.*
637 *Sci.* 136 (1997) 35–39. [https://doi.org/10.1016/S0376-7388\(97\)00149-X](https://doi.org/10.1016/S0376-7388(97)00149-X).
- 638 [5] H. Strathmann, Electrodeialysis, a mature technology with a multitude of new applications, *Desalination.* 264
639 (2010) 268–288. <https://doi.org/10.1016/j.desal.2010.04.069>.
- 640 [6] A. Campione, L. Gurreri, M. Ciofalo, G. Micale, A. Tamburini, A. Cipollina, Electrodeialysis for water
641 desalination: A critical assessment of recent developments on process fundamentals, models and applications,
642 *Desalination.* 434 (2018) 121–160. <https://doi.org/10.1016/j.desal.2017.12.044>.
- 643 [7] J.-M. Arana Juve, F.M.S. Christensen, Y. Wang, Z. Wei, Electrodeialysis for metal removal and recovery: A
644 review, *Chem. Eng. J.* 435 (2022) 134857. <https://doi.org/10.1016/J.CEJ.2022.134857>.
- 645 [8] B. Sun, M. Zhang, S. Huang, Z. Cao, L. Lu, X. Zhang, Study on mass transfer performance and membrane
646 resistance in concentration of high salinity solutions by electrodeialysis, *Sep. Purif. Technol.* 281 (2022)
647 119907. <https://doi.org/10.1016/J.SEPPUR.2021.119907>.
- 648 [9] J. Kim, S. Yoon, M. Choi, K.J. Min, K.Y. Park, K. Chon, S. Bae, Metal ion recovery from electrodeialysis-
649 concentrated plating wastewater via pilot-scale sequential electrowinning/chemical precipitation, *J. Clean.*
650 *Prod.* 330 (2022) 129879. <https://doi.org/10.1016/J.JCLEPRO.2021.129879>.
- 651 [10] T.P. Malalagama, T. Binghui, K.B.S.N. Jinadasa, D.R. Samaraweera, F. Yang, Removal of Fluoride in Water
652 and Wastewater Using Electrodeialysis/Electrodeialysis Reverse Process: A Review, *Lect. Notes Civ. Eng.* 174
653 (2022) 553–564. https://doi.org/10.1007/978-981-16-4412-2_43.
- 654 [11] K.N. Lee, S.M. Donovan, B. Gila, al -, A. Li, Z. Huang, H. Xu, V.S. H Sujoto, W. Astuti, F.R. Mufakhir,
655 H.T. B M Petrus, Lithium recovery from synthetic geothermal brine using electrodeialysis method, *IOP Conf.*
656 *Ser. Earth Environ. Sci.* 882 (2021) 012003. <https://doi.org/10.1088/1755-1315/882/1/012003>.
- 657 [12] L. Gurreri, A. Tamburini, A. Cipollina, G. Micale, CFD analysis of the fluid flow behavior in a reverse
658 electrodeialysis stack, *Desalin. Water Treat.* 48 (2012) 390–403.
659 <https://doi.org/10.1080/19443994.2012.705966>.
- 660 [13] M.R. Cruz-Díaz, A. Laureano, F.A. Rodríguez, L.F. Arenas, J. J. H. Pijpers, E.P. Rivero, Modelling of flow
661 distribution within spacer-filled channels fed by dividing manifolds as found in stacks for membrane-based
662 technologies, *Chem. Eng. J.* 423 (2021) 130232. <https://doi.org/10.1016/J.CEJ.2021.130232>.
- 663 [14] W. Li, P. Hrnjak, Single-phase flow distribution in plate heat exchangers: Experiments and models, *Int. J.*
664 *Refriger.* 126 (2021) 45–56. <https://doi.org/10.1016/J.IJREFRIG.2021.01.026>.
- 665 [15] S. Maharudrayya, S. Jayanti, A.P. Deshpande, Flow distribution and pressure drop in parallel-channel
666 configurations of planar fuel cells, *J. Power Sources.* 144 (2005) 94–106.
667 <https://doi.org/10.1016/J.JPOWSOUR.2004.12.018>.
- 668 [16] A. Muhana, D.R. Novog, Validation of FLUENT for Prediction of Flow Distribution and Pressure Gradients
669 in a Multi-Branch Header Under Low Flow Conditions, *Int. Conf. Nucl. Eng. Proceedings, ICONE.* 2 (2009)
670 221–226. <https://doi.org/10.1115/ICONE16-48128>.
- 671 [17] R.J. Kee, P. Korada, K. Walters, M. Pavol, A generalized model of the flow distribution in channel networks
672 of planar fuel cells, *J. Power Sources.* 109 (2002) 148–159. [https://doi.org/10.1016/S0378-7753\(02\)00090-3](https://doi.org/10.1016/S0378-7753(02)00090-3).

- 673 [18] J. Wang, Pressure drop and flow distribution in parallel-channel configurations of fuel cells: U-type
674 arrangement, *Int. J. Hydrogen Energy*. 33 (2008) 6339–6350.
675 <https://doi.org/10.1016/J.IJHYDENE.2008.08.020>.
- 676 [19] J. Wang, Pressure drop and flow distribution in parallel-channel configurations of fuel cells: Z-type
677 arrangement, *Int. J. Hydrogen Energy*. 35 (2010) 5498–5509.
678 <https://doi.org/10.1016/J.IJHYDENE.2010.02.131>.
- 679 [20] M.K. Bassiouny, H. Martin, Flow distribution and pressure drop in plate heat exchangers—I U-type
680 arrangement, *Chem. Eng. Sci.* 39 (1984) 693–700. [https://doi.org/10.1016/0009-2509\(84\)80176-1](https://doi.org/10.1016/0009-2509(84)80176-1).
- 681 [21] B. Kumar, S.N. Singh, Study of pressure drop in single pass U-type plate heat exchanger, *Exp. Therm. Fluid
682 Sci.* 87 (2017) 40–49. <https://doi.org/10.1016/J.EXPTHERMFLUSCI.2017.04.028>.
- 683 [22] S. Al-Zahrani, M.S. Islam, S.C. Saha, Comparison of flow resistance and port maldistribution between novel
684 and conventional plate heat exchangers, *Int. Commun. Heat Mass Transf.* 123 (2021) 105200.
685 <https://doi.org/10.1016/J.ICHEATMASSTRANSFER.2021.105200>.
- 686 [23] I. Rubinstein, E. Staude, O. Kedem, Role of the membrane surface in concentration polarization at ion-
687 exchange membrane, *Desalination*. 69 (1988) 101–114. [https://doi.org/10.1016/0011-9164\(88\)80013-4](https://doi.org/10.1016/0011-9164(88)80013-4).
- 688 [24] Y. Tanaka, Limiting current density of an ion-exchange membrane and of an electro dialyzer, *J. Memb. Sci.*
689 266 (2005) 6–17. <https://doi.org/10.1016/J.MEMSCI.2005.05.005>.
- 690 [25] Y. Tanaka, A computer simulation of continuous ion exchange membrane electro dialysis for desalination of
691 saline water, *Desalination*. 249 (2009) 809–821. <https://doi.org/10.1016/J.DESAL.2009.04.011>.
- 692 [26] Y. Tanaka, A computer simulation of feed and bleed ion exchange membrane electro dialysis for desalination
693 of saline water, *Desalination*. 254 (2010) 99–107. <https://doi.org/10.1016/J.DESAL.2009.12.008>.
- 694 [27] A. Tamburini, M. Renda, A. Cipollina, G. Micale, M. Ciofalo, Investigation of heat transfer in spacer-filled
695 channels by experiments and direct numerical simulations, *Int. J. Heat Mass Transf.* 93 (2016) 1190–1205.
696 <https://doi.org/10.1016/J.IJHEATMASSTRANSFER.2015.11.034>.
- 697 [28] C.P. Koutsou, S.G. Yiantsios, A.J. Karabelas, Direct numerical simulation of flow in spacer-filled channels:
698 Effect of spacer geometrical characteristics, *J. Memb. Sci.* 291 (2007) 53–69.
699 <https://doi.org/10.1016/J.MEMSCI.2006.12.032>.
- 700 [29] S. Pawlowski, V. Geraldès, J.G. Crespo, S. Velizarov, Computational fluid dynamics (CFD) assisted analysis
701 of profiled membranes performance in reverse electro dialysis, *J. Memb. Sci.* 502 (2016) 179–190.
702 <https://doi.org/10.1016/j.memsci.2015.11.031>.
- 703 [30] J. Veerman, J.W. Post, M. Saakes, S.J. Metz, G.J. Harmsen, Reducing power losses caused by ionic shortcut
704 currents in reverse electro dialysis stacks by a validated model, *J. Memb. Sci.* 310 (2008) 418–430.
705 <https://doi.org/10.1016/j.memsci.2007.11.032>.

706